Variable Switching Point Predictive Torque Control

Petros Karamanakos*, Peter Stolze†, Ralph Kennel†, Stefanos Manias*, and Toit Mouton‡
*Department of Electrical and Computer Engineering, National Technical University of Athens, Athens, Greece
Email: *petkar@central.ntua.gr, manias@central.ntua.gr
†Institute for Electrical Drive Systems and Power Electronics, Technische Universität München, München, Germany
Email: †peter.stolze@tum.de, ralph.kennel@tum.de
‡Department of Electrical and Electronic Engineering, University of Stellenbosch, Stellenbosch, South Africa
Email: ‡dtmouton@sun.ac.za

***Abstract*—In this paper an approach to include a variable switching time point into predictive torque control (PTC) is introduced. In PTC the switching frequency is limited by the sampling frequency; its theoretical maximum value is half the sampling frequency. In reality, however, the switching frequency is lower than this value, resulting in high current and torque ripples compared to modulator-based control methods. In order to overcome this an optimization problem is formulated and solved in real-time. The goal is to find the time point at which the switches of the inverter should change state in order to not only achieve the regulation of the torque and the flux magnitude to their references, but also the minimization of the torque ripple. Further advantages of the proposed method include the design flexibility and great performance during transients. Experimental results that verify the performance of the presented control strategy are included.**

I. Introduction

Nowadays, field oriented control (FOC) [1] and direct torque control (DTC) [2], [3] are considered as two well established methods in three-phase electrical drives control. FOC is a modulation-based approach with a coordinate transformation from stator fixed to a rotor flux oriented coordinate system. In contrast to that, DTC is a direct control approach; the state of the switches is selected from a lookup table, depending on the stator flux angle and the outputs of hysteresis controllers for flux and torque. As it is implied from the absence of a modulator, DTC shows a faster transient response than FOC but has higher current, flux and torque ripples.

Despite the fact that there are more than 25 years that model predictive control (MPC) has been applied to control of electrical drive systems [4], it has just recently been gaining more popularity. Thanks to the advent of more powerful microprocessors, approaches in the framework of MPC become more and more promising. In general, MPC-based algorithms can be divided into modulator-based and into enumeration-based methods [5]–[7]. A famous modulator-based approach is generalized predictive control (GPC) [8], [9]. For electrical drive systems MPC algorithms have been developed on a theoretical level [10], [11], and experimentally verified showing remarkable performance [12], [13].

Another famous MPC approach for flux and torque control of electrical drives is predictive torque control (PTC) [14], [15]. Despite the fact that the concept is similar to that of DTC, it offers more flexibility in the design process. Instead of using hysteresis bounds and lookup tables, an optimization problem is formulated that captures the control objectives, i.e. the regulation of the torque and flux magnitude to their reference values, in a straightforward manner. In addition, constraints like current limitation can be explicitly imposed. Compared to DTC, PTC is a more intuitive approach showing similar favorable behavior during transients. Furthermore, the PTC approach can be easily extended to multilevel inverters [16], [17].

However, the torque and current ripples that PTC delivers are still very high compared to FOC with the same sampling time. In the medium- and high-voltage drives field these large ripples are less important than a low switching frequency of the inverter. The higher the power range of a drive system is, the more dominant are the switching losses in relation to the total losses. Because of this, most of the MPC-based algorithms are better suited for bigger drives and partly they were developed in order to keep the switching frequency as low as possible. In contrast to this, for smaller drive systems the switching losses are less important than a good quality of the torque and the current. By achieving a higher switching frequency these drawbacks can be overcome. In order to reach a higher switching frequency which is in the range of FOC, though, the sampling time has to be decreased; this leads to higher hardware requirements and costs for the whole drive system. A detailed comparison of FOC, DTC and PTC can be found in [18] and [19].

A solution to reduce the torque ripple is to allow the switchings to take place in between the sampling interval. In this way the ripple can be decreased without the need of a further reduction of the sampling time. However, the maximum switching frequency is still limited to half the sampling frequency. In [20] a method to calculate an optimal switching time point for PTC and a permanent magnet synchronous motor (PMSM) is presented.

In this paper a new algorithm for the determination of a variable switching time point for PTC of induction motors

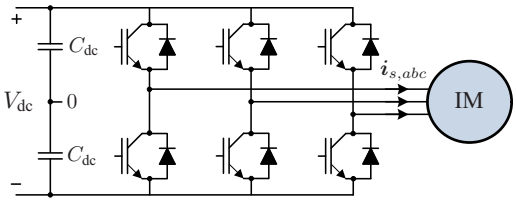

Fig. 1: Two-level voltage source inverter driving an IM.

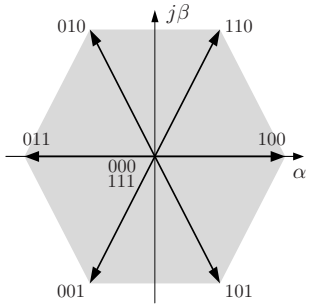

Fig. 2: Voltage vectors of a two-level voltage source inverter and the corresponding switch states.

(IMs) is introduced. The variable switching point is the result of an optimization problem formulated to minimize the torque ripple. The advantages of the proposed method, among others, include the design simplicity, the fast dynamics that MPC can provide, and the inherent robustness. Furthermore, since the prediction horizon is kept as short as possible, i.e. $N = 1$, the computational complexity of the proposed approach is limited, making its implementation in a drive system possible. Finally, thanks to its flexibility it can be easily extended to different types of machines and be adapted for other control tasks.

II. Physical System

A. Two-Level Inverter

Fig. 1 shows the three-phase inverter connected to an IM. The two IGBTs in each one of the three phases are complementary, i.e. if the upper switch is *off*, the lower switch has to be turned *on* and vice versa. In each phase the inverter produces voltages $-0.5V_{\text{dc}}$, and $0.5V_{\text{dc}}$, where V_{dc} is the dc-link voltage. This leads to eight different switching possibilities; modeling the switch state with the variables $u_a, u_b, u_c \in \{0, 1\}$, where "1" corresponds to the case of the positive phase voltage, and "0" to the case of the negative voltage, eight possible combinations of the switch states $\boldsymbol{u}_{abc} = [u_a \ u_b \ u_c]^T$ are produced.

Using the Clarke transformation matrix

$$\boldsymbol{K} = \frac{2}{3}\begin{bmatrix} 1 & -\frac{1}{2} & -\frac{1}{2} \\ 0 & \frac{\sqrt{3}}{2} & -\frac{\sqrt{3}}{2} \end{bmatrix}, \tag{1}$$

the actual voltages applied to the machine terminals are transformed from the abc plane to the $\alpha\beta$ plane resulting in seven unique voltage vectors $\boldsymbol{v}_{\alpha\beta}$ (Fig. 2) given by

$$\boldsymbol{v}_{\alpha\beta} = V_{\text{dc}}\boldsymbol{K}\boldsymbol{u}_{abc}\,. \tag{2}$$

Finally, the switch states $[0\ 0\ 0]^T$ and $[1\ 1\ 1]^T$ are called zero switch states and produce zero voltage vectors, while the others are the active switch states that produce active voltage vectors.

B. Induction Machine

In order to derive a mathematical model appropriate for the controller, the dynamics of the IM are modeled in the stator $\alpha\beta$ reference frame. As state variables are considered the stator current $\boldsymbol{i}_s$, the rotor flux $\boldsymbol{\psi}_r$, and the rotor rotational speed ω_r. The continuous-time state equations are [21]

$$\tau_\sigma \frac{d\boldsymbol{i}_s}{dt} + \boldsymbol{i}_s = \frac{1}{r_\sigma}\boldsymbol{v}_s + \frac{k_r}{r_\sigma}\Big(\frac{1}{\tau_r} - j\omega_r\Big)\boldsymbol{\psi}_r \tag{3a}$$

$$\tau_r \frac{d\boldsymbol{\psi}_r}{dt} + \boldsymbol{\psi}_r = j\omega_r\boldsymbol{\psi}_r + l_m\boldsymbol{i}_s \tag{3b}$$

$$\frac{d\omega_r}{dt} = \frac{1}{J}\big(T_e - T_\ell\big) \tag{3c}$$

where the stator voltage $\boldsymbol{v}_s$ is in the stator $\alpha\beta$ reference plane. Based on the model parameters, i.e. the stator r_s and the rotor r_r resistances, and the stator l_s, the rotor l_r and the mutual l_m inductances, the coefficients in (3) are given as $\tau_\sigma = \sigma l_s/r_\sigma$, $r_\sigma = r_s + k_r^2 r_r$, with $k_r = l_m/l_r$, $\tau_r = l_r/r_r$, and $\sigma = 1 - l_m^2/(l_s l_r)$. Variable J stands for the inertia, T_ℓ for the mechanical load torque, and the electromagnetic torque T_e is given by

$$T_e = \frac{3}{2}p\big(\boldsymbol{\psi}_s \times \boldsymbol{i}_s\big)\,. \tag{4}$$

In (4) p is the number of pole pairs, and $\boldsymbol{\psi}_s$ is the stator flux vector

$$\boldsymbol{\psi}_s = \sigma l_s \boldsymbol{i}_s + \frac{l_m}{l_r}\boldsymbol{\psi}_r\,, \tag{5}$$

the magnitude of which is given by

$$\Psi_s = \sqrt{\psi_{s\alpha}^2 + \psi_{s\beta}^2}\,. \tag{6}$$

In a subsequent step eqs. (3) to (5) are discretized using Euler forward approximation. The discretized state-space model of the machine is of the form

$$\boldsymbol{x}(k+1) = (\boldsymbol{I} + \boldsymbol{A}T_s)\boldsymbol{x}(k) + \boldsymbol{B}T_s\boldsymbol{u}(k) \tag{7a}$$

$$\boldsymbol{y}(k) = \boldsymbol{C}\boldsymbol{x}(k) \tag{7b}$$

where the state vector is selected to be $\boldsymbol{x} = [i_{s\alpha}\ i_{s\beta}\ \psi_{s\alpha}\ \psi_{s\beta}]^T$, the switch states $\boldsymbol{u}_{abc}$ serve as the input vector, and the output vector is $\boldsymbol{y} = [T_e\ \Psi_s]^T$. The matrices $\boldsymbol{A}$, $\boldsymbol{B}$ and $\boldsymbol{C}$ are the continuous-time matrices which can easily be calculated using elementary linear algebra. Finally, $\boldsymbol{I}$ is the identity matrix and T_s is the sampling interval.

III. Variable Switching Point Predictive Torque Control (VSP^{2}TC)

In this work MPC is used to control the output variables, i.e. the torque and the magnitude of the stator flux. Furthermore, an additional control objective is the reduction of the torque ripple. Based on PTC introduced in [14] and [15] the proposed algorithm aims to meet both control objectives without a significant increase of the switching frequency. This is achieved by solving an optimization problem in real-time; a variable switching point is calculated within the prediction horizon of a fixed length based on the minimization of the torque ripple.

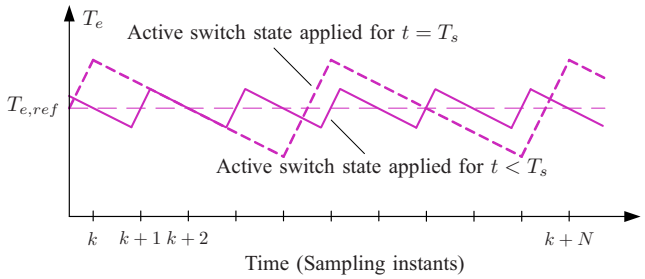

Fig. 3: Principle of the proposed strategy for torque ripple reduction.

A. Control Problem

In direct switching strategies such as DTC and PTC high torque ripples occur, since a switch state is applied for at least one sampling interval T_s. An active switch state leads to higher current and torque ripples compared to the zero switch state. Hence, if it could be applied for a time period t less than one sampling interval $t < T_s$, then the torque ripple could be reduced.

This principle is shown in Fig. 3, where for reasons of simplicity only two switch states are assumed to be applied: an active switch state resulting in a high positive torque slope, and a zero switch state resulting in a low negative slope. As it can be seen, the active switch state leads to a high ripple; the longer it is applied, the higher the ripple. If the switching could take place *in between* the sampling interval, the switch state that results in the high ripple would be applied for less time; in this way the ripple could be reduced. However, as it can be observed in Fig. 3, this leads to a higher switching frequency. It should be mentioned, though, that this higher switching frequency can be achieved with the same sampling time. Furthermore, for both cases, the maximum switching frequency is limited to half the sampling frequency, as each IGBT can switch only once during one sampling interval T_s.

B. Control Algorithm

By selecting a switch state at a time instant within the sampling interval, i.e. $kT_s \leq (k + n_{int}^{(k)})T_s \leq (k+1)T_s$, where the superscript k denotes the k^{th} interval, and $n_{int}^{(k)} \in [0, 1]$, rather than at the beginning of each interval $\big(kT_s, (k+1)T_s, \ldots, (k+N)T_s\big)$, with $N \in \mathbb{N}^+$, the goal is to reduce the torque ripple. The procedure for the calculation of the variable switching point comprises the following steps, executed at step k.

Step 1: At step k the switch state calculated at the previous sampling interval $\boldsymbol{u}(k-1+n_{int}^{(k-1)})$ is applied.

Step 2: According to (7b), the electromagnetic torque at time instant kT_s is calculated from the measurements of the stator currents and the rotor speed. Using (7a), and by applying the same switch state $\boldsymbol{u}(k) = \boldsymbol{u}(k-1+n_{int}^{(k-1)})$ for the entire sampling interval T_s, the predicted values of the stator current, the stator and the rotor flux are calculated; based on these values the torque at step $k+1$ is computed. Considering a constant torque slope, m, for one T_s, the following affine (linear plus offset) expression describes the relationship between the torque at step k and at $k+1$ (Fig. 4(a))

$$T_e(k+1) = T_e(k) + m(k)T_s\,. \tag{8}$$

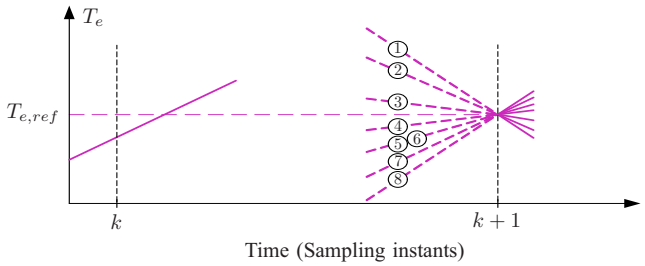

(a) The torque at k is calculated based on the applied switch state $\boldsymbol{u}(k) = \boldsymbol{u}(k-1+n_{int}^{(k-1)})$. Seven unique torque trajectories that correspond to the eight different switch states are calculated at $k+1$.

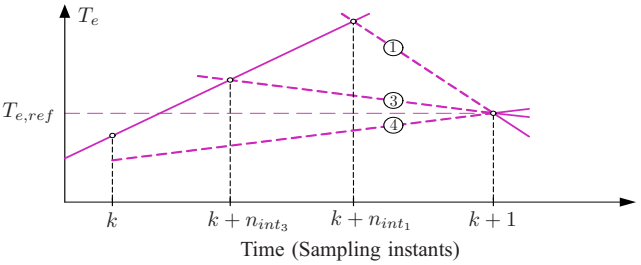

(b) The point where the torques of steps k and $k+1$ intersect is calculated. Here, three out of seven candidate torque trajectories are shown; torques (1) and (3) at $k+1$ intersect with $T_e(k)$, while torque (4) does not.

Fig. 4: A variable switching point is calculated in order to minimize the torque slope. In (a) the calculation of the torque slopes and in (b) the calculation of the variable switching point are shown.

Step 3: The predicted state and output variables are recomputed assuming that the switch state at step k can be anyone out of the eight possible. The corresponding torque slopes are calculated according to the modified (8)

$$T_{e_z}(k+1) = T_e(k) + m_z(k)T_s\,, \tag{9}$$

with $z \in \{0, 1, \ldots, 7\}$ denoting the selected switch state. Since $T_s \ll T_1$, where T_1 is the fundamental period, the torque slopes can be considered as, without loss of generality, to remain the same for the successive sampling interval, i.e. $m_z(k) = m_z(k+1)$, see Fig. 4(a).

Step 4: Setting as goal the torque to reach its reference value at step $k+1$, the variable switching point $n_{int}^{(k)}$ is calculated: the intersection between the trajectory of the actual torque $T_e(k)$ and each one of the *possible* trajectories of the calculated torque $T_{e_z}(k+1)$ is computed; its projection onto the time axis equals to the variable switching point (Fig. 4(b)). Hence, the variable switching point is given by:

$$t_z = \frac{T_{e,ref} - T_e(k) - m_z(k+1)T_s}{m(k) - m_z(k+1)}\,, \tag{10}$$

where t_z is the projection of the intersection point T_{e,int_z}, resulting from the z switch state, onto the x-axis, i.e. $t_z = n_{int_z}^{(k)} T_s$[1]. The torque at the intermediate step is $T_{e,int_z} = T_{e_z}(k + n_{int_z}^{(k)})$.

Step 5: By taking into account the variable switching point, the predicted values of the state and output variables are

[1]The switching point can, theoretically, be in the range $t_z \in (-\infty, +\infty)$. However, it is limited in the range $t_z \in [0, T_s]$, with "0" corresponding to PTC.

calculated at step $k + n_{int_z}^{(k)}$. This means that in (7) t_z is used instead of T_s. Following, the predictions of the variables of interest are computed for each switch state, in a similar manner as before, with the difference that now the corresponding time interval $T_s - t_z$ is used instead of t_z.

Step 6: In a last step an objective function is formulated and it is minimized in real-time. The chosen function is:

$$J(k) = \sum_{\xi \in \mathcal{S}} \Big(||T_{e,ref} - T_e(k+\xi|k)||_2^2 + \\ + \lambda ||\Psi_{s,ref} - \Psi_s(k+\xi|k)||_2^2 \Big) . \tag{11}$$

In (11) the squared 2-norm[2] is chosen in order to penalize more heavily the deviations from the reference values. Furthermore, the set $\mathcal{S}$ is defined as $\mathcal{S} = \{n_{int}, 1\}$. Finally, the weighting factor $\lambda > 0$ sets the trade-off between the electromagnetic torque error and the stator flux magnitude error.

Subsequently, by taking into account the objective function (11) and the system dynamics (7) an optimization problem is formulated:

$$\begin{aligned} &\text{minimize} \quad J(k) \\ &\text{subject to} \quad \text{eq. (7)} . \end{aligned} \tag{12}$$

The underlying optimization problem is solved in real-time every T_s. The switch state $\boldsymbol{u}(k)$ that results in the minimum associated cost is considered to be the optimal solution, i.e. $\boldsymbol{u}^*(k)$, and it is applied to the inverter at time instant $(k + n_{int}^{(k)})T_s$.

Finally, at the next time-step, the whole procedure is repeated with new measurements or estimates.

C. Delay Compensation

In digital control systems a delay exists between the time instant that measurements are made and the time instant that these values are delivered to the controller. This comes from the fact that the algorithm cannot be executed in zero time. Considering that for the implementation of VSP^{2}TC in a drive system, a delay of one sample has to be taken into account. This means that this delay can be compensated by adding one prediction in order to achieve the best possible results.

IV. Performance Evaluation

The proposed algorithm was tested in the laboratory. Fig. 5 shows the experimental setup which consists of two 2.2 kW squirrel-cage IMs. One of the motors is used as load machine, driven by a Danfoss VLT FC-302 3.0 kW inverter. The working machine is driven by a modified Seidel/Kollmorgen Servostar 600 14 kVA inverter which allows the user to give the gating signals directly via a suitable control system. The dc-links of both inverters are connected in order to avoid a frequent use of the break chopper resistor. The real-time computer with a 1.4 GHz Pentium CPU used for the experiments is described in [22]. The machine speed is measured via a 1024 points incremental encoder. Both algorithms were executed with a sampling time $T_s = 61.44\,\mu$s.

[2]The p-norm, with $p \geq 1$ is defined as $||x||_p = (|x_1|^p + \ldots + |x_n|^p)^{1/p}$.

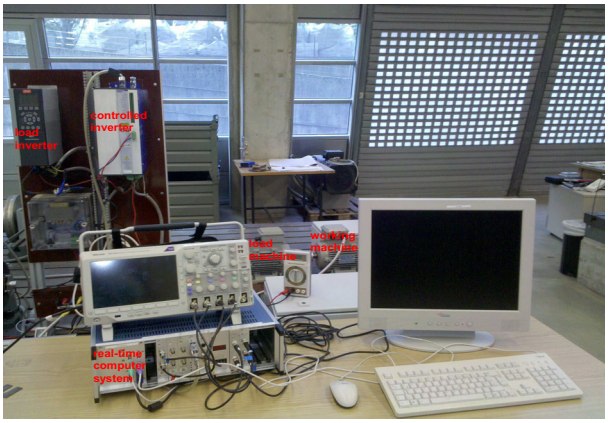

Fig. 5: Experimental setup including the two coupled squirrel-cage IMs (back), the two inverters (left) and the real-time computer system used for control (front).

TABLE I: Parameters of the experimental setup

Parameter	Value
Sampling time T_s	61.44 μs
dc-link voltage V_{dc}	582 V
Number of pole pairs p	1
Stator resistance r_s	2.6827 Ω
Rotor resistance r_r	2.1290 Ω
Stator inductance l_s	283.4 mH
Rotor inductance l_r	283.4 mH
Mutual inductance l_m	275.1 mH

Table I shows the parameters of the experimental setup. The parameters of the working machine were measured with the Danfoss load inverter.

A. Steady-State Operation

Firstly, the steady-state performance of the drive was examined for both VSP^{2}TC and PTC. For PTC the objective function was chosen to be as the one presented in [15], i.e.

$$J(k) = \big(T_{e,ref} - T_e(k+1)\big)^2 + \lambda \big(\Psi_{s,ref} - \Psi_s(k+1)\big)^2 . \tag{13}$$

The drive operates at half nominal speed, i.e. the fundamental frequency is $f_1 = 25$ Hz. The torque reference is set equal to $T_{e,ref} = 4$ Nm, and the stator flux magnitude reference to $\Psi_{s,ref} = 0.7$ Wb. The results are presented in Figs. 6 and 7 for VSP^{2}TC and PTC, respectively. As it can be seen in Figs. 6(a) and 7(a), where the three phase stator currents are depicted, the VSP^{2}TC produces currents of lower total harmonic distortion (THD $= 3.15\%$, Fig. 6(b)) than these which PTC delivers (THD $= 4.11\%$, Fig. 7(b)). However, it should be mentioned that the switching frequency is not the same for both approaches, despite the fact that for both experiments the same sampling time is used. For VSP^{2}TC the switching frequency is around $f_{sw} \approx 3.2$ kHz, while for PTC it is around $f_{sw} \approx 2.9$ kHz. That slight mismatch occurs because of the nature of the proposed strategy, as already explained in Section III. The possibility for the inverter to select a different switch state within the interval leads to higher switching frequencies.

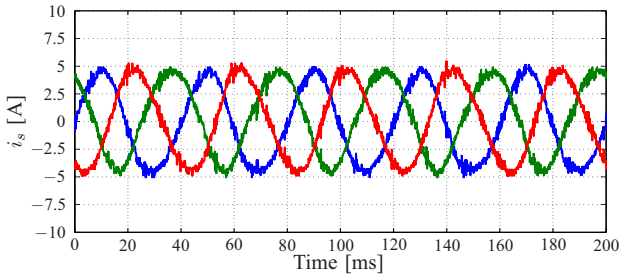

(a) Three-phase stator currents.

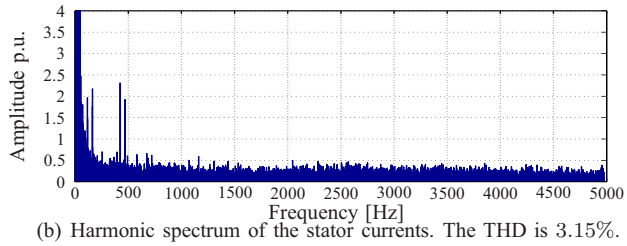

(b) Harmonic spectrum of the stator currents. The THD is 3.15%.

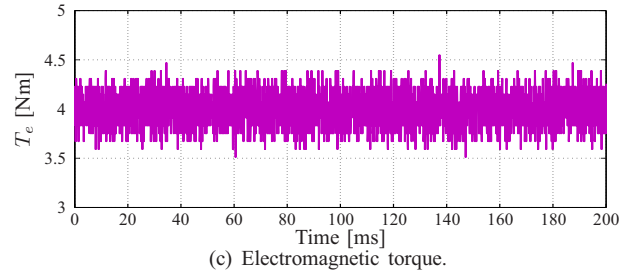

(c) Electromagnetic torque.

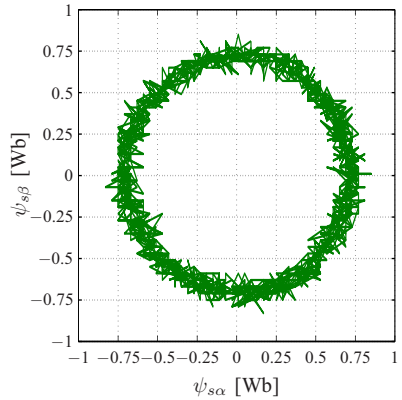

(d) Flux in $\alpha\beta$ plane.

Fig. 6: Experimental results of the proposed control strategy (VSP^{2}TC) for steady-state operation at half nominal speed ($f_1 = 25$ Hz). The switching frequency is $f_{sw} \approx 3.2$ kHz.

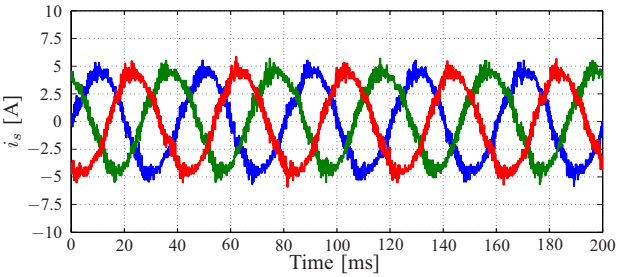

(a) Three-phase stator currents.

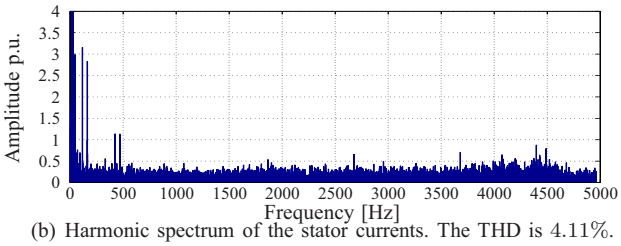

(b) Harmonic spectrum of the stator currents. The THD is 4.11%.

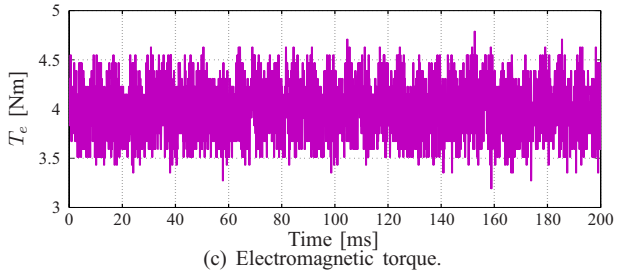

(c) Electromagnetic torque.

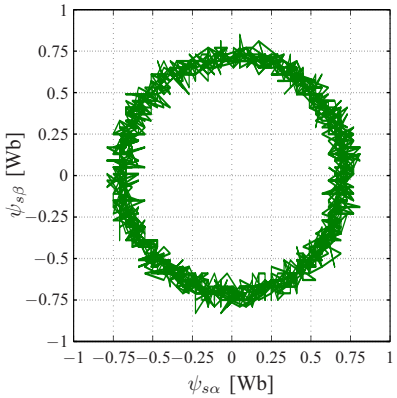

(d) Flux in $\alpha\beta$ plane.

Fig. 7: Experimental results of the predictive torque control (PTC) for steady-state operation at half nominal speed ($f_1 = 25$ Hz). The switching frequency is $f_{sw} \approx 2.9$ kHz.

The results of the optimization over the torque ripple are presented in Fig. 6(c). As it is clearly shown, the proposed control strategy results in a significantly reduced torque ripple compared to PTC (Fig. 7(c)). Finally, the stator flux in the $\alpha\beta$ plane is depicted in Figs. 6(d) and 7(d); the flux stator magnitude is equal to the reference.

B. Torque Step Change Response

The performance of VSP^{2}TC during transients was also tested; the result is shown in Fig. 8. A step-up change in the torque reference takes place at $t \approx 3$ ms from $T_{e,ref} = 2$ Nm to $T_{e,ref} = 4$ Nm. The controller reacts very fast to the reference torque change and rejects the disturbance in less than 0.5 ms (Fig. 8(a)). Furthermore, as it can be seen in Fig. 8(b), the flux remains unaffected by the reference torque change. Finally, the torque response (Fig. 9(a)) for the same scenario was examined when the drive is controlled with PTC. Similar dynamic performance is observed, since the torque reaches its new reference value very fast, too.

V. Conclusions and Future Work

In this paper a control algorithm, namely the variable switching point predictive torque control (VSP^{2}TC), was intro-

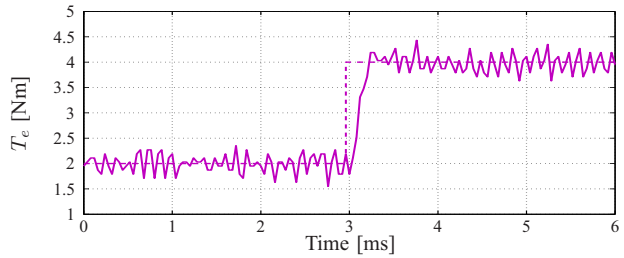

(a) Electromagnetic torque (solid line) and its reference value (dashed line)

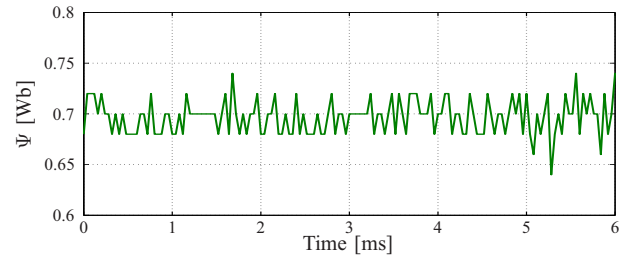

(b) Flux magnitude.

Fig. 8: Experimental results with VSP^{2}TC for a step change of the electromagnetic torque at $t \approx 3\,\text{ms}$.

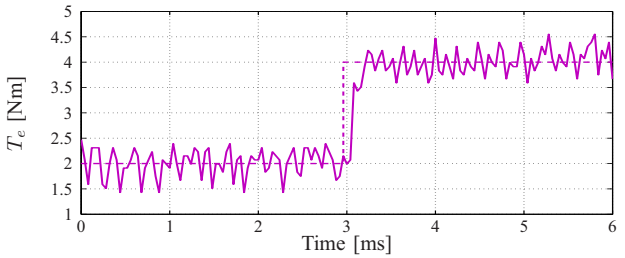

(a) Electromagnetic torque (solid line) and its reference value (dashed line)

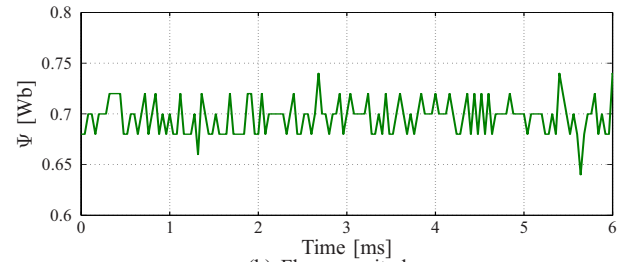

(b) Flux magnitude.

Fig. 9: Experimental results with PTC for a step change of the electromagnetic torque at $t \approx 3\,\text{ms}$.

duced. By selecting a different switch state within the sampling interval the controller aims to reduce the torque ripple, while achieving zero steady-state torque and stator flux tracking errors. The VSP^{2}TC method comes with a slightly increased switching frequency compared to PTC. However, this is not a major disadvantage; for drive systems up to a few kW where switching losses are not so important, the proposed method can significantly improve the control result. Furthermore, the design simplicity and flexibility of the controller implies that this method could be easily extended to other topologies, such as three-level neutral point clamped and flying capacitor inverters. Experimental results are presented to demonstrate the favorable performance of VSP^{2}TC under steady-state and transient operating conditions.

References

[1] M. P. Kazmierkowski, R. Krishnan, and F. Blaabjerg, *Control in Power Electronics*. New York: Academic Press, 2002.

[2] M. Depenbrock, "Direct self-control (DSC) of inverter-fed induction machines," *IEEE Trans. Power Electron.*, vol. 3, no. 4, pp. 420–429, Oct. 1988.

[3] I. Takahashi and T. Noguchi, "A new quick-response and high-efficiency control strategy of an induction motor," *IEEE Trans. Ind. Appl.*, vol. IA-22, no. 5, pp. 820–827, Sep. 1986.

[4] J. Holtz and S. Stadtfeld, "A predictive controller for the stator current vector of AC-machines fed from a switched voltage source," in *Int. Power Electron. Conf.*, vol. 2, Tokyo, Japan, Mar. 1983, pp. 1665–1675.

[5] A. Linder, R. Kanchan, P. Stolze, and R. Kennel, *Model-based Predictive Control of Electric Drives*. Göttingen: Cuvillier Verlag, 2010.

[6] T. Geyer, "Low complexity model predictive control in power electronics and power systems," Ph.D. dissertation, Automatic Control Laboratory ETH, Zurich, 2005.

[7] P. Cortés, M. P. Kazmierkowski, R. M. Kennel, D. E. Quevedo, and J. Rodríguez, "Predictive control in power electronics and drives," *IEEE Trans. Ind. Electron.*, vol. 55, no. 12, pp. 4312–4324, Dec. 2008.

[8] D. W. Clarke, C. Mohtadi, and P. S. Tuffs, "Generalized predictive control—Part I. The basic algorithm," *Automatica*, vol. 23, no. 2, pp. 137–148, Mar. 1987.

[9] ——, "Generalized predictive control—Part II. Extensions and interpretations," *Automatica*, vol. 23, no. 2, pp. 149–160, Mar. 1987.

[10] T. Geyer, G. Papafotiou, and M. Morari, "Model predictive direct torque control—Part I: Concept, algorithm and analysis," *IEEE Trans. Ind. Electron.*, vol. 56, no. 6, pp. 1894–1905, Jun. 2009.

[11] T. Geyer, N. Oikonomou, G. Papafotiou, and F. Kieferndorf, "Model predictive pulse pattern control," *IEEE Trans. Ind. Appl.*, vol. 48, no. 2, pp. 663–676, Mar./Apr. 2012.

[12] G. Papafotiou, J. Kley, K. G. Papadopoulos, P. Bohren, and M. Morari, "Model predictive direct torque control—Part II: Implementation and experimental evaluation," *IEEE Trans. Ind. Electron.*, vol. 56, no. 6, pp. 1906–1915, Jun. 2009.

[13] N. Oikonomou, C. Gutscher, P. Karamanakos, F. Kieferndorf, and T. Geyer, "Model predictive pulse pattern control for the five-level active neutral point clamped inverter," in *Proc. IEEE Energy Convers. Congr. Expo.*, Raleigh, NC, Sep. 2012, pp. 129–136.

[14] P. Correa, M. Pacas, and J. Rodríguez, "A predictive torque control for inverter-fed induction machines," *IEEE Trans. Ind. Electron.*, vol. 54, no. 2, pp. 1073–1079, Apr. 2007.

[15] H. Miranda, P. Cortés, J. I. Yuz, and J. Rodríguez, "Predictive torque control of induction machines based on state-space models," *IEEE Trans. Ind. Electron.*, vol. 56, no. 6, pp. 1916–1924, Jun. 2009.

[16] P. Stolze, M. Tomlinson, D. du Toit, R. Kennel, and T. Mouton, "Predictive torque control of an induction machine fed by a flying capacitor converter," in *Proc. IEEE Conf. Africon*, Livingstone, Zambia, Sep. 2011, pp. 1–6.

[17] P. Stolze, F. Bauer, P. Landsmann, R. Kennel, and T. Mouton, "Predictive torque control of an induction machine fed by a neutral point clamped inverter," in *Proc. Workshop on Pred. Control on Electr. Drives and Power Electron.*, Munich, Germany, Oct. 2011, pp. 24–29.

[18] R. Kennel, J. Rodríguez, J. Espinoza, and M. Trincado, "High performance speed control methods for electrical machines: An assessment," in *Proc. IEEE Int. Conf. Ind. Technol.*, Viña del Mar, Chile, Mar. 2010, pp. 1793–1799.

[19] J. Rodríguez, R. Kennel, J. R. Espinoza, M. Trincado, C. A. Silva, and C. A. Rojas, "High-performance control strategies for electrical drives: An experimental assessment," *IEEE Trans. Ind. Electron.*, vol. 59, no. 2, pp. 812–820, Feb. 2012.

[20] P. Landsmann and R. Kennel, "Saliency-based sensorless predictive torque control with reduced torque ripple," *IEEE Trans. Power Electron.*, vol. 27, no. 10, pp. 4311–4320, Oct. 2012.

[21] J. Holtz, "The representation of AC machine dynamics by complex signal flow graphs," *IEEE Trans. Ind. Electron.*, vol. 42, no. 3, pp. 263–271, Jun. 1995.

[22] N. Al-Sheakh Ameen, A. A. Naassani, and R. M. Kennel, "Design of a digital system dedicated for electrical drive applications," *EPE J.*, vol. 20, no. 4, pp. 37–44, Dec. 2010.